Materials Advances

Accepted Manuscript

This article can be cited before page numbers have been issued, to do this please use: S. Bhattacharya, I. A. Kühne, T. Ohto and H. Tada, *Mater. Adv.*, 2025, DOI: 10.1039/D5MA00565E.

ROYAL SOCIETY OF CHEMISTRY

rsc.li/materials-advances

View Article Online
DOI: 10.1039/D5MA00565E

ARTICLE

Evolution of Giant Exchange Bias with Ferromagnetic Ordering and Robust Memory Effect by Strain Engineering MoS_2 in Weak Antiferromagnetic Gating

Received 00th January 20xx,
Accepted 00th January 20xx

DOI: 10.1039/x0xx00000x

Shatabda Bhattacharya,*[a,b] Irina A. Kühne[b], Tatsuhiko Ohto[c] and Hirokazu Tada[a]

The emergence of 2D ferromagnetism in MoS_2 layers induced by an inherently non-magnetic material like NiOOH is an interesting area of research. This result is of widespread technological importance if additionally associated with magnetic exchange correlations that shows promising memory effects. In this work, we show that a giant exchange bias is housed within a highly strained 2D MoS_2 multilayers by interfacing thin weakly antiferromagnetic β-NiOOH phase. The robustness and magnitude of such zero-field-cooled exchange bias emerges from the unique sublattice spin configuration of β-NiOOH which serves as a source of surface uncompensated moments, while highly strained 2D MoS_2 acts as active pinning layer in the hybrid. The exchange coupling between the weak antiferromagnetic layer and the adjacent moment induced ferromagnetic layer is strong enough to show near room temperature thermoremnant (TRM) memory effect in the magnetization states which is newly observed for 2D hybrid materials. Upon manifesting vertical type junction, this hybrid material also shows non-volatile electrical bistable states with low operating bias voltage (1.25V) and high ON/OFF ratio (6×10^2) along with hysteretic magnetoresistance which can be useful in 2D based spintronic applications. First principle calculations also verified such charge transfer interactions at the interace of the hybrid structure.

1. Introduction

The correlated properties in quantum hybrid materials are one of the most interesting areas of research in nanotechnology where properties from the individual components are coupled together. In this area, transition metal dichalcogenides (TMDs) have unique 2D van der Waals structure with absence of dangling bonds and layer dependent properties such as band gap tunability, mobility variation, strain engineering those can possibly combined with other type of materials.[1] MoS_2, a promising one such TMD has attracted enormous interest for its recent potential application in transistors, catalysis, optoelectronic devices etc..[2-7] Due to the layer type structure, it can withstand large strain before braking and thus strain engineering has become a hot topic of research.[8] This strategy is now wisely used to tune the property of MoS_2 based semiconducting devices. Additionally, benefitted with the valley band-specific spins, the strong spin-orbit interaction in such materials is an additional parameter to control its electronic states. Despite of such properties, due to absence of inherent magnetism in MoS_2, the incorporation of magnetism into TMDs has proposed to integrate spin-valley interaction in 2D materials. Different from direct magnetic doping, the use of magnetic proximity effect (MPE) where an adjacent magnetic layer is employed to induce the effect is considered as an eminent strategy to gain long range magnetic interactions in hybrid heterostructures.[9-11] In such context, so far ferromagnetic materials are only used for this MPE effect using conducting type of metallic materials. However, for transport related properties, the magnetic conductors may short circuit the adjacent MoS_2 layer in proximity and ultimately restrict the electrical measurement of the hybrids. In this case, other than conducting type, antiferromagnetic insulators can be a possible substituent to this to understand the coupling effect. Since antiferromagnets have two antiparallel spin orientations, the effect of interfacial coupling is to generate induced magnetic moment in the nearby 2D template via charge transfer effect. For example, in graphene case, when transition metals (TM) are placed in proximity to graphene surface, induced moment is observed in 2D layers but the 3d orbital moment of TM is quenched due to hybridization.[12,13] Particularly, when nickel is used for inducing moment in 2D surfaces (graphene, germanene or silicone), then it is found due to a secondary charge transfer from metal's 4s orbital to its 3d orbital, nickel can be transformed into diamagnetic which becomes detrimental.[14-16] Apart from these issues, the question of formation of metal oxide when exposed the 2D-hybrid to open atmosphere is a long standing problem. In TMDs, due to the sulfur rich environment, it is more prone to interact with the nearby metal-complexes of suitable types to stabilize structures.

[a] Department of Materials Engineering Science, Graduate School of Engineering, Osaka University, Toyonaka, 560-8531, Osaka, JAPAN
[b] Division of Condensed Matter Physics, FZU-Institute of Physics of the Czech Academy of Sciences, Na Slovance 1999/2, 182-00, Prague, CZECH REPUBLIC
[c] Graduate School of Engineering Science, Nagoya University, Furo-cho, Chikusa-ku, Nagoya, Aichi 464-8603, JAPAN
E-mail: shatabda@fzu.cz
Supplementary Information available: See DOI: 10.1039/x0xx00000x

View Article Online
DOI: 10.1039/D5MA00565E

Despite the induction of weak ferromagnetic ordering in intrinsically non-magnetic MoS_2 by highly magnetic insulators (yttrium iron garnets: YIG) or TMs (Fe, Co, Ni) is quite observable, the role of non-magnetic metal-oxides are relatively unexplored.[17] Interest for the nickel hydroxide ($Ni(OH)_2$) and it's redox pair i.e. NiOOH for the last century due to their excellent catalytic activity, battery applications, cathode material etc. have grown interest.[18-20] The derivative of structures can be commonly called as NiOx. The structure of NiOOx can remain in basically four phases such as: β-$Ni(OH)_2$, α-$Ni(OH)_2$, β-NiOOH and γ-NiOOH.[21-22] The main characteristics of these four phases are they each consists of primary NiO_2 slabs with tetrahedral coordination of H-atoms in between interslab space which makes them interesting.[23] While α-$Ni(OH)_2$ and γ-NiOOH are poorly crystallized with turbostratic disorder, β-$Ni(OH)_2$ and β-NiOOH are relatively stable in nature.[24,25] Majority of literature says that oxidation of β-$Ni(OH)_2$ to β-NiOOH leaves it in a similar hydrogen bonded structure with space group of $P\bar{3}m1$.[26,27] Being a more primitive and fundamentally important material, the presence of partial Ni^{3+} state or a mixture of Ni^{2+} and Ni^{4+} in a disproportionate manner could be interesting to find its magnetic behaviour when attached to 2D surface and how it can alter the magnetic state to its nearby 2D layer.[28]

In this manuscript, we report ultrathin layers of the antiferromagnetic β-NiOOH phase (height variation ~ 5-20nm), grown on a multi-layered MoS_2 surface. We have investigated the interfacial effect by tuning the number of layers. The β-phase of NiOOH is a layered structure where the weak antiferromagnetic interactions arise at low temperatures due to superexchange coupling between the Ni^{3+} centres through oxygen. The β-phase of NiOOH with its unique partial presence of Ni^{3+} oxidation state (in distorted octahedra) is relatively unexplored in the area of its fundamental magnetic states i.e. ground spin state condition and magnetic applications.[29] The antiferromagnetic phase induces a magnetic moment in the adjacent MoS_2 via interfacial coupling effect which results in large coercive fields (~ 6439 Oe) and ferromagnetic long-range interaction (~20 fold rise in magnetization moment) with high Curie temperature in the hybrid nanostructure. The structural mismatch generates a large tensile microstrain (~10^{-2}) in this 2D MoS_2-hybrid, which is thoroughly characterized by X-ray Rietveld method for micro-strain analysis, Transmission electron microscope (TEM) and RAMAN spectra. Due to its high zero field cooled (ZFC) exchange bias effect (~ 1500 Oe) in a 2D MoS_2 based hybrid, it has been extensively tested for high-density magnetic storage devices via thermo-remanent magnetization procedures and found exotic robustness (over long-time scales 25,000 s) as magnetic storage application, including voltage mediated magnetic switching as bistable memory states. This hybrid material further showed a rewritable non-volatile electrical memory with energy efficient low switching bias voltage (<1.25 V) and high current ON-OFF ratio (~10^2) compared to its conventional counter parts. The ON/OFF ratio enhances to 6×10^2 upon field bias using this 2D MoS_2 based hybrid material as active layer in vertical type junctions. Such observed large ON/OFF-ratio is effective to eliminate the probability of misreading during memory testing.[30-33] The electrical bi-stability is highly voltage dependent resembling a reading-writing process in vertical layered memory analogue. During the density functional theory calculation of MoS_2-βNiOOH composites, we found FM ordering for monolayer of β-NiOOH on 2D MoS_2 whereas for bilayer of β-NiOOH, which can be also considered as thick sample, AFM interaction was found to be in the ground state. Also at the interface, bader charge analysis showed finite value of charge transfer. Hence the 2D layer is responsible for changing the magnetic state of adjacent NiOOH layers.

Despite long term study of a suitable prototypical exchange bias system, layered AFM/2D heterostructure could give a complete understanding of the cause behind this large exchange bias effect. The pinned uncompensated surface moments in the AFM phase are interacted within the interface of highly disordered MoS_2 defect lattice via coupling effect. Frustration that emerges due to site disorder or competition among local exchange interactions are the main criteria of this kind of interaction, resulting interesting two-step magnetization and sizable exchange bias (EB) effect in 2D hybrid. The strong coupling between AFM β-NiOOH layer and charge transfer induced FM layer generate such high ZFC EB effect. It is found that due to such structure formation, highly field responsive, pinned moments are embedded within the 2D matrix that shows a dependence of magnetic moment upon thermal cycles which is known as thermoremanent magnetic memory effect as studied in an extensive way to undemand the spin dynamics of the hybrid 2D heterostructure.[34-36]

2. Results and discussion

A. Synthesis and Structural characterizations of MoS_2/β-NiOOH hybrids

The synthesis process was carried out in two steps. In the first step, MoS_2 has been prepared under hydrothermal conditions as follows. As a source for Molybdenum, we used hexaammonium heptamolybdate tetrahydrate [$(NH_4)_6Mo_7O_{24} \cdot 4\ H_2O$; 5mM=310mg] and as a sulfur source, we used thiourea (70mM=268 mg) and dissolved in 40ml of DI water under vigorous stirring forming a homogenous solution. This mixture was sealed in a Teflon lined (PTFE) stainless steel autoclave maintaining a temperature of 180 °C for 24h. After this reaction, the black product, which is the suspended MoS_2 layers were thoroughly washed with water and ethanol several times to eliminate unreacted molecules or excess sulfur and collected finally via centrifuge methods (10000 rpm). As we have prepared two different batches of the hybrid samples, the stock solution of parent MoS_2 was equally divided into two parts and dissolved in 50 ml anhydrous N,N-Dimethylformamide (n-DMF) (dense solvent) for ultrasonication of 2h. During this time, the MoS_2 layers were exfoliated by the ultrasonic vibration and well dispersed in the solution.

To this MoS_2 solution (50ml), 50ml nickel acetate ($Ni(OAc)_2$) aqueous solution (concentration of Ni salt 0.1 M) was added with urea (0.002M) and 0.1g of polyvinyl pyrrolidone (PVP). The resulting mixture was refluxed at 50 °C for 1h and subsequently added 1M of

View Article Online
DOI: 10.1039/D5MA00565E

NaOH solution (20ml). The final solution was set to autoclave for 100 ^{o}C 24h. The final product was washed with water, ethanol and acetone subsequently to remove excess unreacted products of urea and PVP. They were dried under vacuum in 40^{o} C. According to the concentration of Ni, sample was named as MN-1 (high concentration of NiOOH). We prepared another batch of sample with same MoS_2 but the Nickel precursor salt was (0.01M) i.e. 1/10th to MN-1 and is termed as MN-2 (lower concentration of NiOOH). The concentration of initial nickel precursor salt was directly proportion to the layer thickness of the formed nanoflakes of the NiOOH structure over MoS_2.

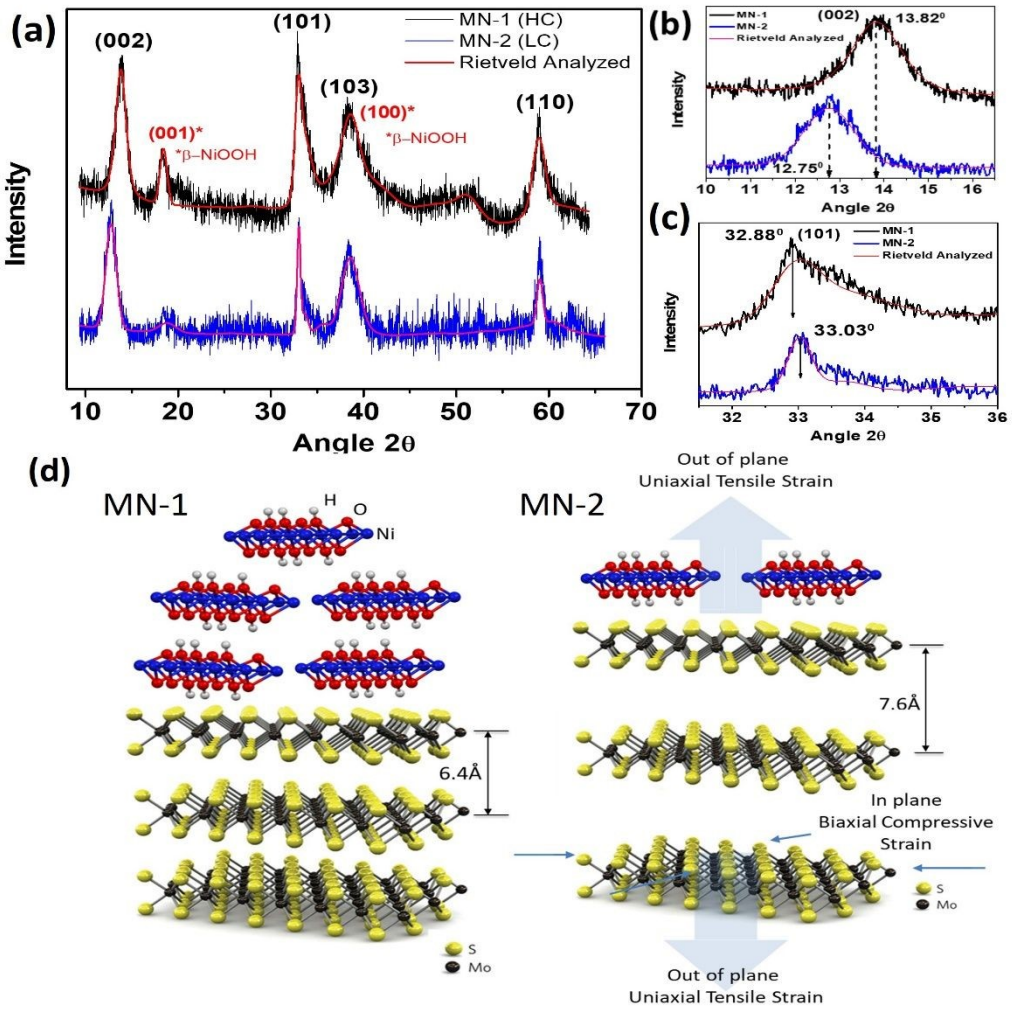

Fig. 1: (a) *powder XRD profiles of the composite samples MN-1 and MN-2 respectively with the characteristics MOS_2 and β-NiOOH peaks. Red line is the Rietveld fitted data.* ***(b)*** *magnified view of the (002) MoS_2 layer separation peaks from the previous plot.* ***(c)*** *magnified view of the (100) peaks for the two composites.* ***(d)*** *schematic diagram of the two different morphologies of the β-NiOOH phase on the layered structure of MoS_2. Interlayer separation has been increased due to out-of-plane tensile strain in the heterostructures.*

B. X-ray diffraction (XRD) and Rietveld refinement analysis of the composites:

Powder XRD of the two nanocomposites were carried out and obtained the profile as shown in **Fig. 1a,b** for MN-1 and MN-2 respectively. To analyse the structure pattern and strain in the composites, we fitted the experimental data using MAUD^{TM} program for Rietveld fitting.[37-38] The characteristics MoS_2 peaks represent hexagonal symmetry ($P6_{3/mmc}$) and β-NiOOH phase trigonal symmetry ($P\bar{3}m1$). The peaks were further matched with JCPDS card numbers 37-1492 (for MoS_2) and 6-0141 for β-NiOOH phase, respectively. The red line curve corresponds to Rietveld fitted to the experimental graph and Table I shows the extracted parameters viz. lattice constants, R.M.S microstrain, crystallite size, structure equivalency etc. From the overall XRD profile, it is seen that the peak intensity for the MoS_2 phase remains almost unchanged for the two samples, while the main peak of β-NiOOH phase, i.e. (001) changes its intensity as layer number is diminished from MN-1 to MN-2 sample. There is also large shift of (002) plane of MoS_2 from 13.82^{0} (MN-1) to 12.75^{0} (MN-2) due to interlayer tensile strain in MoS_2 along c-axis ([001] direction) due to which the interlayer separation has expanded (Fig. 1a). It is to be noted that for MoS_2, the (002) planes may expand due to intercalation but in this case, it is due to the out of plane uniaxial tensile strain because of heterostructure growth expanding interlayer spacing (c-axis) as found in literature by Yang et. Al.[39]. Later in TEM analysis of cross-sectional views of (002) MoS_2 planes, no signature of chemical intercalation was found. Whereas the peak of (101) plane of MoS_2 shifts to a larger angle 2θ i.e., from 32.88^{0} (for MN-1) to 33.03^{0} (for MN-2), indicating in-plane biaxial compressive strain (Fig. 1c) and schematic of Fig. 1d for MN-2

sample.[39] This fact is also visualized in TEM images and analyses given later for the strain effects in the basal planes of MoS_2. From the **Table I** of Rietveld refinement, if we carefully look at the c-lattice parameter of MoS_2, it changes from 12.72 Å (MN-1) to 13.76 Å (MN-2). Microstrain value calculated from the Rietveld refinement analysis for MoS_2 phase increases from -0.008 (MN-1) to -0.059 (MN-2) which is enormously high for strain parameter in 2D systems [40,41]. In-case of β-NiOOH phase, there is also microstrain changes from 0.009 (MN-1) to 0.029 (MN-2), and the 'a'-lattice parameter squeezes from 3.07 Å (MN-1) to 2.25 Å (MN-2) which is a compressive strain for β-NiOOH phase. From this analysis it can be concluded that for MN-2 sample, the strain is much higher than MN-1 due to thin layer of β-NiOOH layer and the overall MoS_2 layers are also highly strained in MN-2 sample. Fig. 1d shows a schematic diagram of the MoS_2/ β-NiOOH heterostructures where for MN-1 sample (left), thick layer of β-NiOOH is grown on MoS_2 surface with interlayer separation of MoS_2 about 6.4Å and in MN-2, thin layers of β-NiOOH is shown with out-of-plane tensile strain [001] direction, that expands the interlayer separation of MoS_2 with 7.6 Å and highly strained structure is formed. Additionally, it is pertinent to mention that around 38.5^0 for MoS_2, (103) plan is very weak in intensity if it comes from only MoS_2 phase, but as it is overlapped here with NiOOH (100) position, it is increased in intensity. [42, 43]

Table I: XRD parameters obtained after Rietveld refinement of the p-XRD data of the two composite samples

Phase	Thick layer over MoS_2 (MN-1)			Thin layer over MoS_2 (MN-2)		
MoS_2	Lattice parameters	Value	Error (±)	Lattice parameters	Value	Error (±)
	a,b	3.13Å	0.002	a,b	3.12 Å	0.003
	c	12.72 Å	0.003	c	13.76 Å	0.004
	microstrain	-0.008	3.2×10^{-5}	microstrain	-0.059	4.4×10-4
β-NiOOH	Lattice parameters	Value	Error (±)	Lattice parameters	Value	Error (±)
	a,b	3.07 Å	0.003	a,b	2.25 Å	0.002
	C	4.78 Å	0.005	c	4.69 Å	0.001
	microstrain	-0.007	0.01×10^{-5}	microstrain	-0.028	1.9×10^{-4}

C. Transmission electron microscopy (TEM) image analysis for the growth structure

Fig. 2a, shows the MN-1 sample with overall image of β-NiOOH layers overlapping largely on the MoS_2 surface. The right upper inset part shows magnified β-NiOOH nanodisc. The left upper part is the selected area electron diffraction (SAED) pattern from the overall structures showing multiple diffraction spots for a large number of overlapped NiOOH layers at different angles as observed previously [44]. Next in **Fig. 2b**, the basal plane of MoS_2 is shown in high resolution (HR) mode, where the highly strained 2D layer structure can be seen in the yellow circle spotted areas with noticeable localized dark patches with disrupted lattice continuity usually seen for highly strained 2D layer systems. The in-plane MoS_2 surface is highly strained as evidenced from this high resolution (HR) TEM image, also found during many cases.[45,46] Next, for MN-2 sample, comparatively thinner layers of β-NiOOH nanodisc are shown. MoS_2 remained as a substrate with low contrast area in the background (**Fig. 2c**). The upper right inset of **Fig. 2c** shows the magnified view of the overlapped β-NiOOH layers (1~3) where the thin film morphology of NiOOH is highlighted. The left upper inset (Fig. 2c) is the corresponding SAED diffraction pattern with only a few bright spots which depicts the low number of layers in NiOOH. In **Fig. 2d**, the HR cross-sectional view of the MoS_2 interlayer planes (002) are given for the two concentrations of the composite MN-1 (left) and MN-2 (right) respectively with the histogram plot in the center as analyzed from the IMAGE-J software, showing the quantitative average layer spacing in Å for MoS_2 in the two composites .[47]

For MN-1, the average separation of (002) MoS_2 layer is about 6.4 Å which in good agreement with typical normal 2-H type MoS_2-layer spacing of 6.45Å.[48] Whereas, for the MN-2 nanocomposite, MoS_2 the interlayers are expanded, and the average interlayer separation comes as 7.6 Å due to high out-of-plane uniaxial tensile strain generated (along [001] direction) in the hybrid structures with much more strain and defects.[49] The (002) plane spacing highly depends on strain, defects, intercalation or exfoliation. In our case, there is no effect from intercalation and hence the expansion and distortion are primarily due to strain effect discussed here in detail with more TEM cross-sectional and basal planar microstructural images. Infact, intercalated structures (if any) would have been seen in the (002) planes in the cross-sectional view, which is absent here. [50, 51] From the separation between the peaks in the histogram plot of the interlayers (middle figures), it can be understood how the layers are expanded, counting 8 peaks for MN-1 and 6 peaks for MN-2 within a similar uniform lateral distance scale-range of (002) planes (middle of Fig. 2(d)).

In **Fig. 2f**, we have shown another in-plane high resolution lattice image of the MN-2 composite, where lattice fringe bending is sharply observed as a result of NiOOH growth and strain effect involvement [52, 53]. Upon further magnifying in the yellow coloured highlighted part in **Fig. 2g**, lattice fringe bending and waviness are observed throughout the in-plane TEM image of the composite, especially near the center. These are indicative of local in-plane, bi-axial strain and lattice distortion in 2D materials maybe due to substrate mismatch, interfacial stress due to composite growth[39]. Lattice fringes are clearly bended and formed twining boundaries as highlighted in yellow circled regions **(Fig. 2 g).** In a large view of the cross-sectional image of MN-2, in **Fig. 2h**, fringe compression/expansion showing non-uniform fringe spacing that lead to local variation in (002) interlayer spacing. Dislocation faults in (002) layers are marked specifically with yellow-colored circles (Fig. 2h) forming by point defects or vacancy clusters altering interlayer interaction[54]. This interprets out-of-plane strain i.e. perpendicular to (002) plane. Not only this, edge dislocation or stacking faults are seen among (002) interlayer planes highlighted with yellow dots as the planes merged or dislocated, shown in **Fig. 2h**. Hence from the TEM analysis a clear picture of the overall growth morphology and surface defects are

View Article Online
DOI: 10.1039/D5MA00565E

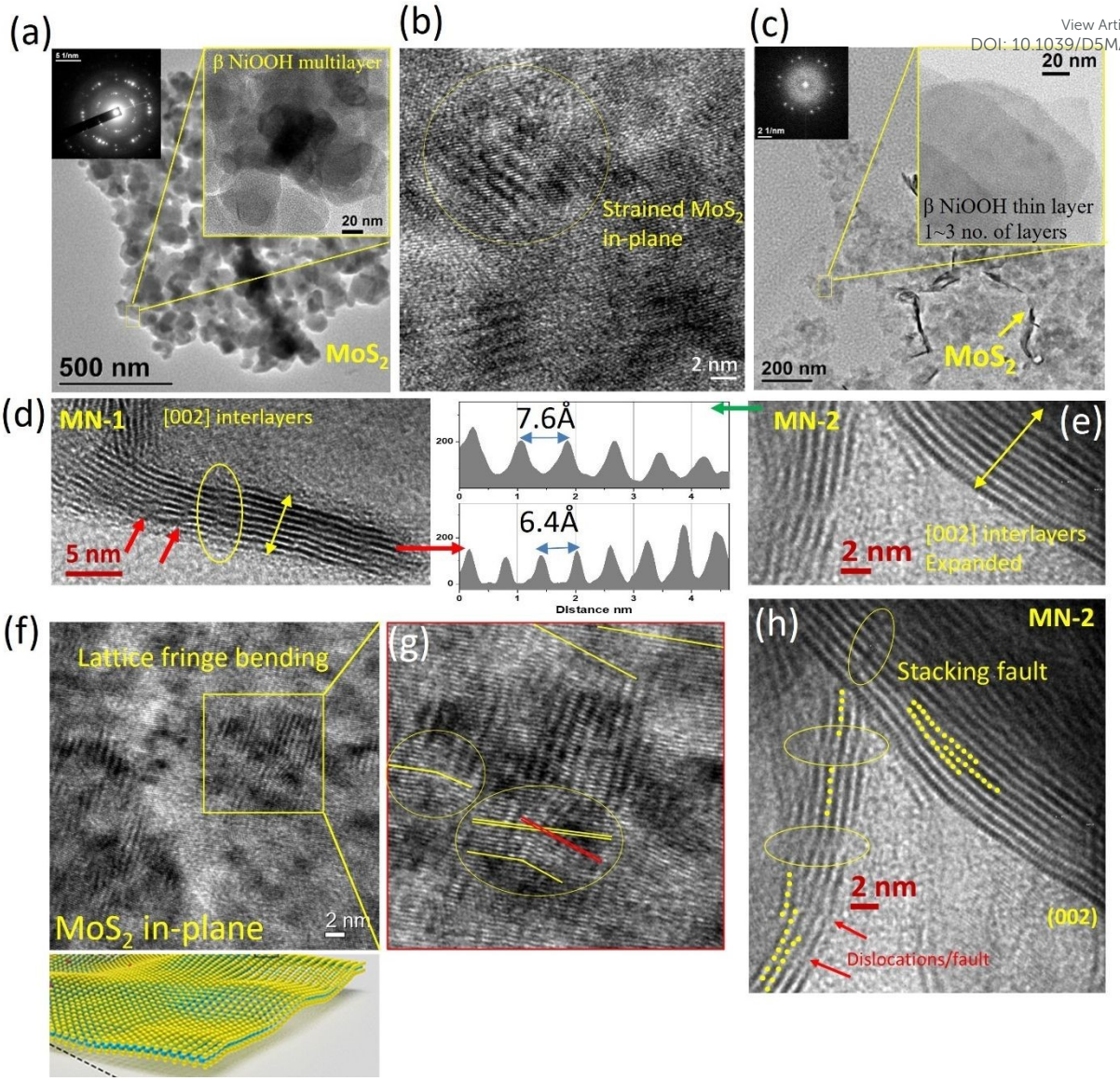

Fig. 2: (a) *Overall TEM morphology of MN-1 composite with inset showing overlapped β-NiOOH nanodisc. SAED multispot confirms layered type structure.* ***(b)*** *high resolution magnified view of the highly strained MoS2 in-planes due to the formation of heterostructure.* ***(c)*** *overall morphology of the MN-1 samples with inset shows magnified view of the thin layers of β-NiOOH phase.* ***(d)*** *left (MN-1) magnified view of (002) MoS2 interlayers with corresponding plot of histogram in center. The average peak separation is the interlayer distance between MoS_2 layers i.e. 6.4 Å. (e) Right: For MN-2 composite, the (002) interlayers are expanded (7.6 Å) with corresponding histogram plot in the centre. (f) in-plane lattice fringe bending of the composite with waving of the layers. (g) magnified view of the in-plane shows local lattice distortion due to strain and bending in fringes, growth in different orientations. Local dark patches verify strain effect in MoS2. (h) overall view of the MN-2 cross-sectional (002) plane with stacking fault and dislocations/faults highlighted by yellow circles.*

identified in the 2D surfaces along with the thin nanodiscs as observed in typical microstructural analysis. [52-54]

D. Raman spectral analysis of vibrational modes of MoS_2 due to strain:

MoS_2 exhibits only weak bonds between the stacked S-Mo-S layers which are held together by the van der Waals' forces.[55] Out of different atomic vibrational modes in MoS_2, the out-of-plane A_{1g} mode (Sulfur atoms move in opposite directions perpendicular to the plane, while Mo atoms remain stationary) and in-plane E^1_{2g} mode (Mo and S atoms vibrate in opposite directions within the plane.) are the most active ones. The presence of foreign β-NiOOH layer can induce strain in MoS_2 which alters the interlayer interaction and change the characteristics peaks in Raman. The position of $E_{2g}{}^1$ and A_{1g} peaks for pristine MoS_2 phase arise at about 382.9 and 407.7 cm^{-1} as shown in **Fig. 3**. Compared to this, for the nanocomposites MN-1 and MN-2, red shift of both $E_{2g}{}^1$ and A_{1g} modes are observed which is typically due to the strain generated in the MoS_2 planes as found in other literatures also (**Supporting information: Fig. S1 a,b**). [56,57] From Fig. S1 in SI, the shift in $E_{2g}{}^1$ mode is the strongest in MN-2 compared to MN-1 or pristine MoS_2 which is mainly sensitive to strain effect.[56,57] The out-of-plane tensile strain in MoS_2 weakens the interlayer interaction leading to a shift in frequency from the pristine MoS_2 to MN-1 or MN-2 as observed in our case. Furthermore, the

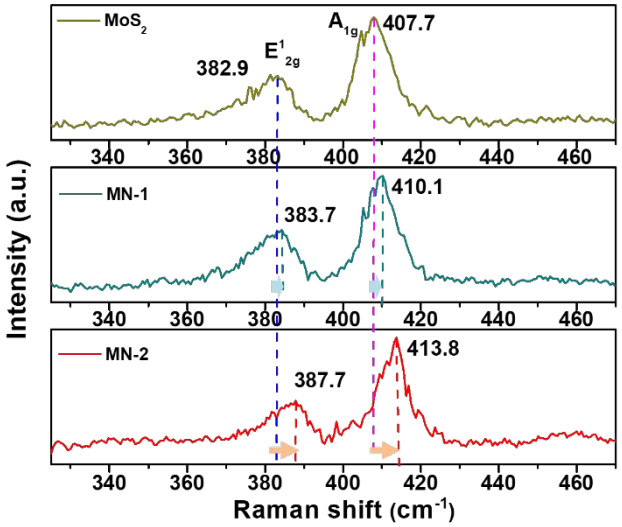

Fig. 3 *RAMAN spectra of the two composites along with pristine MoS_2 phase for comparison of peak shifting and strain analysis. The position of E_{2g} and A_{1g} are shifted with respect to the pure MoS_2 phase, and the dashed line shows the position with shift in the composite samples.*

difference between these two modes i.e., $\boldsymbol{\Delta\omega = A_{1g} - E^1_{2g}}$, (in cm^{-1}) remains almost constant in the case of composites (Fig. S1b). This is due to the fact that the layer number in MoS_2 doesn't change with the samples. This plot is important as with increasing the number of layers in MoS_2, the $E_{2g}{}^1$ mode is red shifted to higher frequency along with the difference between A_{1g} and $E_{2g}{}^1$ is also enlarged, which is not the case here.[29] Hence the initial layer number in MoS_2 remain same for the two different batches of the samples as seen from the Raman studies. However, for both MN-1 and MN-2 composites, the characteristics $E_{2g}{}^1$ and A_{1g} peaks are shifted from the pristine MoS_2 prepared the in the same way. The reason is due to the surface growth of the different NiOOH phase that change the inter layer interaction among the layers in MoS_2 via interface interaction. Hence from the Raman analysis of the two composites along with pristine MoS_2 phase, the strain effect is evidenced due to the noticeable positional change in the characteristic's vibrational modes of MoS_2.

E. Surface topography of the composites by atomic for microscopy (AFM):

Fig. 4a-c shows the contact mode AFM images of the two samples (MN-1 and MN-2) that depict the height profile of the grown nanostructures of the composite. Both the samples were measured on SiO_2/Si wafer as a reference substrate for AFM measurement with composite sample drop casted on the wafer and dried well before measurement. Fig. 4a is for MN-1 sample and Fig. 4 b,c are for the MN-2 samples. In Fig. 4a, a typical β-NiOOH nanodisc is shown on top of a multilayered MoS_2 surface for MN-1 phase i.e. thick β-NiOOH layers. To accurately measure the height, we have measured several lines (in different colours) and the height profile vs. lateral dimension are shown sidewise. In the red and blue profile for MN-1 (Fix 4a), a clear step height due to NiOOH phase is observed over MoS_2 with average height of about 20nm. The contrast difference between MoS_2 and β-NiOOH phase can be clearly understood from the top surface morphology images that reveal the difference in the height profiles also. For MN-1, from the AFM image we also calculated the average surface roughness, average height of a large specific area from the histogram plot (Supporting information **SI Fig. S4a**). Quantitative analysis of surface roughness was performed by extracting height distribution histograms from the AFM images using *WSxM software* (See methods in **SI Section S4**). It is found that for MN-1, from the plot in histogram (green colour), average height of 15.81 nm with roughness average of 10.64 nm, surface skewness of 1.74 indicating a predominantly protruding surface with more high features. A surface kurtosis of 5.17 for MN-1 indicating higher probability of isolated topographic irregularities, consistent with thicker NiOOH nucleation and aggregation. Next in **Fig. 4b,c** thin layers of β-NiOOH phase with bottom MoS_2 layer are shown for MN-2 composites where the number of NiOOH layers are smaller that corresponds to thinner phases. In Fig. 4b, for MN-2, sample in a selected area, we measured three different line profiles as shown in green, blue and red colours (on the right side within height profile plots) and found an average height of 4 to 5 nm of β-NiOOH phase from the height profile figure. For this plot, we also have done detail roughness analysis separately as shown in **Supporting Information, section 4, Fig. S4 (b)** with average height of 3.5nm from the histogram plot, with surface roughness of 1.39 nm, surface skewness of 1.89 and surface kurtosis of 7.81. The corresponding spectrum is shown in blue colour on the right side (**SI section 4, Fig. S4 (b)**).

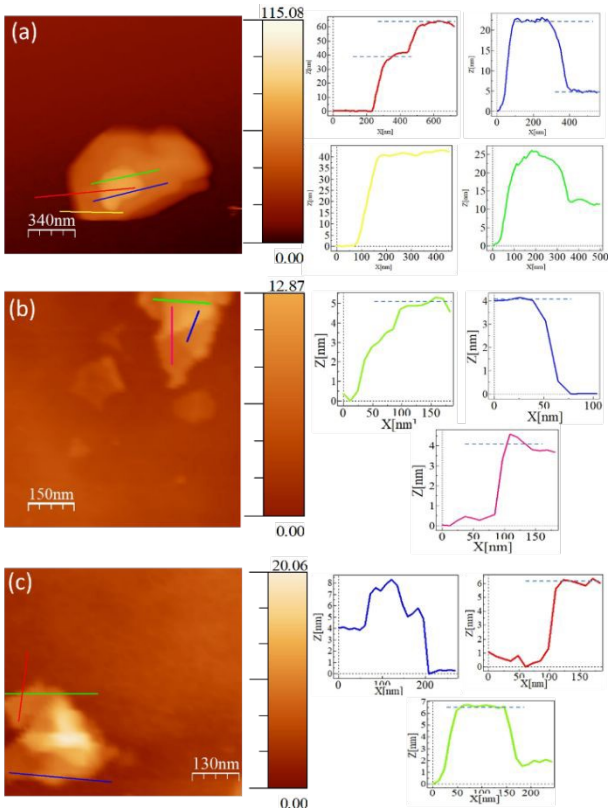

Fig. 4 (a) *AFM image of* ***MN-1*** *with the height profiles of the β-NiOOH layers on right. The step like behavior of the typical multilayered heterostructure (MN-1).* ***(b)*** *for* ***MN-2****, the thin layer of β-NiOOH can be seen with average height profile plot on right.* ***(c)*** *for the overall plot of MN-2, with height profile in inset showing the average thickness of the grown structures. See SI for surface topography detailed analysis section 4.*

Hence, MN-2 samples exhibited a much smoother topography, with an average roughness of 1.39 nm and an average NiOOH flake height of 3.51 nm. These values reflect the presence of ultrathin NiOOH layers or clusters sparsely decorating the MoS_2 surface. In another repeat measurement of MN-2 from the same sample (**Fig. 4C**), the β-NiOOH average height came as ~ 5-6 nm from the height profile plots in different colored lines. For this image in **Fig. 4C**, we also done the roughness analysis (**Fig S4 C, in SI**) with histogram in blue colour, with calculated average height of 5.26 nm, with average surface roughness of 1.75 nm, surface skewness of 2.27 and surface kurtosis of 10.10. The positive skewness in all the samples, Indicates sharp peaks from height profiles, i.e. topologically wrinkles from highly strained MoS_2 layers, dislocation outcrops. On the other hand, kurtosis measures the tailedness or sharpness of height distribution. Here, high kurtosis (>3) denotes presence of sharp features often linked to localized strain, defect pinning or out-of-plane distortions. [58, 59] The elevated skewness and kurtosis parameters in both samples, particularly in MN-2, suggest the presence of localized strain fields and structural inhomogeneities, likely arising from NiOOH–MoS_2 interfacial interactions. [58, 59]

F. X-ray photoelectron spectroscopy analysis of pure MoS_2 and MoS_2 NiOOH composite

In the MoS_2-β-NiOOH composite, as MoS_2 interacts with NiOOH phase at the interface, interesting chemical and electronic interactions such as charge transfer, binding energy change are synergistically detected via X-ray photoelectron spectroscopy (XPS) analysis in this case. We have performed detail XPS study of pure MoS_2 and MoS_2 β-NiOOH composite (MN-2 sample) by drop casting the samples on Si wafer (see **SI Section 5** for details of XPS measurement and protocol). **Fig. S5** in SI shows the overall survey peaks of pure MoS_2 and composites where typical Mo, S, Ni, O and Si peaks are only observed proving purity of the samples.

In the high-resolution Mo 3d core level of pure MoS_2 and MoS_2-NiOOH spectra as shown in **Fig. 5a** with main dual peaks arising from Mo $3d_{3/2}$ and $3d_{5/2}$ were deconvoluted into further two peaks employing Gaussian-Lorentzian mixing. For pure MoS_2, the main Mo $3d_{5/2}$ and $3d_{3/2}$ peaks appeared at around 229.07 and 232.26 eV respectively. While for the composite, the main 3d peaks are shifted to 229.69 and 232.90 eV. The shift is due to the interfacial charge transfer from MoS_2 to NiOOH (Mo becomes more electron-deficient). NiOOH is electrochemically active and can act as electron acceptor due to its oxidative character. Hence electrons can transfer from MoS_2 to NiOOH making Mo become more electron deficient. Also, within each Mo 3d orbital doublets, i-MoS2 peak (purple colour) refers to stoichiometric intrinsic MoS_2 and d-MoS_2 peaks (violet) for defective or sub-stoichiometric part denoting vacancies and defects in MoS_2 [ref 60]. If we compare the pure MoS_2 and MoS_2-NiOOH composite XPS Mo 3d spectra, in the composite, a clear reduction in the contribution of i-MoS_2 (purple area) while increase in the contribution of d-MoS_2 (green area) for the composite is due to more vacancies/defects in the composite [61, 62]. The other peak at around 226 eV is due to S 2s orbital bound to Mo atom in the structure which is usually found.

Next the high resolution, S 2p doublet spectra ($2p_{1/2}$ and $2p_{3/2}$) from the pure MoS_2 and composite MoS_2-NiOOH phase (**shown in Fig 5b**) are further deconvoluted into mainly four peaks. Incase of pure MoS_2, peaks at 164.79 (red colour) and 169.92 eV (blue) are contributed from terminal disulfur S_2^{2-} or sulfur S^{2-} species. While peaks at 163.05 and 161.54 eV are due to apical S^{2-} or bridging S^{2-} (green and yellow) for pure MoS_2.[63, 64] In case of the MoS_2-NiOOH composite, the terminal disulfur S_2^{2-} or sulfur S^{2-} species peaks are shifted to lower binding energies of 163.59 eV (red) and 168.21 eV (blue) with sharped increased intensity for terminal S. It is known that terminal S_2^{2-} is mainly responsible for active binding/interfacial interaction sites in MoS_2 and often lowered in binding energy whenever interacted with nearby complexes as observed in other literatures too.[65, 66]

On the other hand, S peaks for bridging and apical are reduced in intensity for the composite sample in this case. As a result for composite, the S 2p peaks are shifted to overall lower binding energies[63]. Additionally for the composite, the peak appeared at around 170.68 eV may be attributed to S-H interfacial bonds which is found here due to interface interaction.

In β-NiOOH, it contains both Ni^{2+} and Ni^{3+} species, and in XPS, these typically show distinguishable peaks in the Ni 2p region (846-890 eV), often with satellite structures (**Fig. 5c**). It shows multiplet-split peaks due to the interaction between the Ni 2p core and the 3d valence electrons. When MoS_2 interacts with NiOOH, the relative intensities and positions of Ni^{2+} and Ni^{3+} peaks can change, reflecting charge transfer and oxidation state redistribution as found in **Fig. 5c** for the Ni 2p peak of the composite.[67, 68] After deconvolution of the 2p spectra ($2p_{3/2}$ and $2p_{1/2}$), the majority of the intense peaks at around 854.07 and 872.18 eV are due to Ni^{3+} species in NiOOH phase, while the lower binding energy peaks at around 853.42 and 870.81 eV are due to Ni^{2+} species, due to presence of partial $Ni(OH)_2$ phase and reduction by the interfacial charge transfer effect transforming a part of NiOOH to $Ni(OH)_2$ [69, 70]. The Ni satellite peaks are also detected at around 860 and 876 eV (green colour) which are usually observed in Ni 2p spectra. Next, the O 1s spectrum from the composite is shown in **Fig. 5d**. When deconvoluted it appears to be multiple components where the main high intense peak at around 532.21 eV (yellow) is due to OH^- group from NiOOH, small peak at around 530.15 eV is due to lattice O^{2-} correlated to the Ni–O lattice in NiOOH/$Ni(OH)_2$ due to partial reduction as a result of charge transfer, with additional adsorbates peak at higher binding energy of 533.1 eV. Hence, in summary, XPS analysis of the MoS_2-NiOOH heterostructure reveals clear evidence of interfacial interaction and charge transfer from MoS_2 to NiOOH, accompanied by shifts in core-level binding energies and the presence of mixed Ni^{2+}/Ni^{3+} states. Additionally, subtle changes in the S 2p region suggest defect formation, contribution

View Article Online
DOI: 10.1039/D5MA00565E

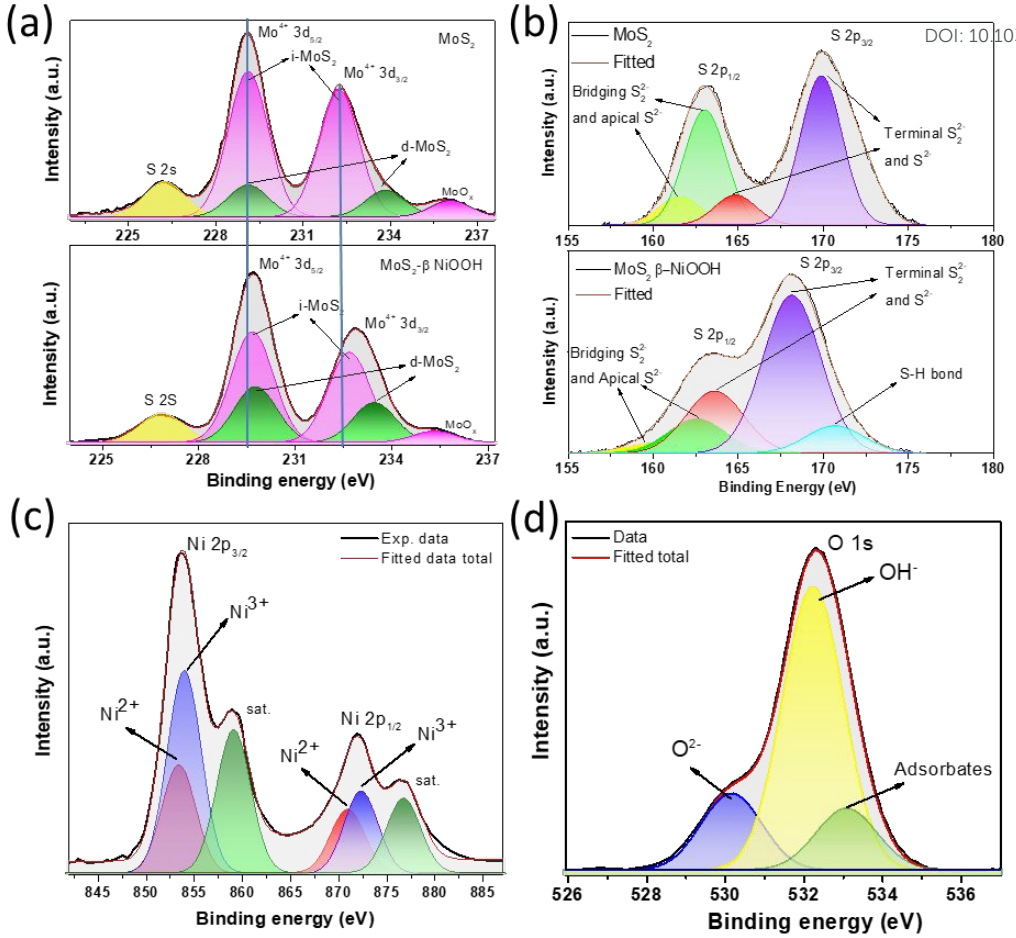

***Figure 5**. (a) Mo 3d orbital XPS spectra of pure MoS_2 (top) and MoS_2-NiOOH composite (bottom) with deconvoluted parts from different components and species with identifications. (b) S 2p orbital XPS spectra of pure MoS_2 (top) and MoS_2-NiOOH composite (bottom) with deconvoluted parts inside for different components. (c) Ni 2p orbital spectra for the composite with deconvoluted components denoting oxidation state of Ni ions. (d) O 1s spectrum from the composite with the deconvoluted parts and contribution from components.*

from different intrinsic (less defective) MoS_2 and defect rich MoS_2 as a result of composite growth and electronic modulation within the orbital binding energy due to interfacial interaction.

3. Magnetic measurements:

A. Spontaneous magnetization curves of the MoS_2 based hybrids:

To understand the intrinsic behavior of the hybrid systems, we carried out zero field cooled (ZFC) and field cooled (FC) magnetization protocols under different dc magnetic fields in the temperature range of 2-300K in a MPMS superconducting quantum interference device (SQUID) magnetometer as shown in **Fig. 6**. For both the samples, large exchange splitting has been observed between FC and ZFC branch up to 300K that proves a strong magnetic ordering in the hybrid system compared to pristine MoS_2 phase where it was absent (See **supporting information Fig. S2**). For thick coverage sample (MN-1), the characteristics antiferromagnetic ordering appeared in the ZFC curves at around 50K, which becomes stronger with increased magnetic field (Inset of **Fig. 6a**). At 100 Oe field, the peak in ZFC was not sharp, so we increased the field strength and at 500 Oe it is prominent to see the change. In the low temperature region, for MN-1, FC branch did not saturate completely due to presence of stronger antiferromagnetic ordering (at low temperatures) among the overlapped β-NiOOH clusters in the Z direction (vertical to the in-plane of MoS_2). From the first order derivative plot of $\Delta(M_{FC}-M_{ZFC})$ (i.e. difference between the magnetizations) in **Fig. 6b**, the ordering temperature (which is T_N in this case) is estimated to be 52K for 500 Oe field. Inset of **Fig. 6b** shows the full variation of $\Delta(M_{FC}-M_{ZFC})$ vs. T with a prominent point of inflection around this temperature. As we tuned (reduced) the thickness of β-NiOOH phase over MoS_2 in the MN-2 sample, the exchange splitting has enormously increased with complete saturation in FC magnetization throughout the temperature range of 100K due to stronger ferromagnetic ordering in the system (**Fig. 6c**). The $\Delta(M_{FC}-M_{ZFC})$ vs. T curve (inset of **Fig. 6d**) shows a uniform variation up to 300K. Interestingly, the specific magnetization moment of the hybrid composite has increased by many folds in MN-2 phase that points induced magnetization in MoS_2 phase in addition to weakly magnetic β-NiOOH phase. For MN-2 at lowest point 2K,

View Article Online
DOI: 10.1039/D5MA00565E

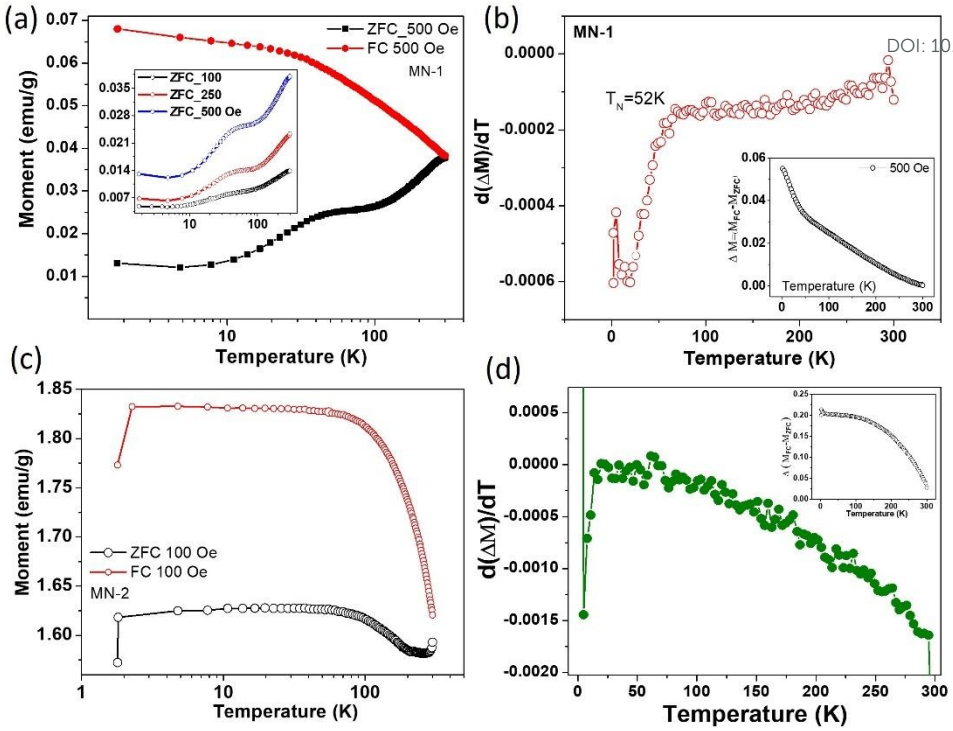

***Fig. 6**: **(a)** ZFC-FC plot of MN-1 during heating cycle. Inset shows effect of increasing magnetic fields on ZFC curves. **(b)** first order derivative plot of $\Delta M(M_{FC}-M_{ZFC})$ with respect to temperature, showing point of inflection at 52K. The inset shows the original difference plot as a function of temperature for MN-1 obtained from ZFC-FC plot. **(c)** ZFC_FC plot for MN-2 with complete saturation at low temperature due to strong ferromagnetic ordering. **(d)** corresponding derivative plot of $\Delta M(M_{FC}-M_{ZFC})$ for MN-2. Inset showing the original difference plot from ZFC_FC curve of MN-2.*

in the ZFC_FC plot, data point lowered maybe due to stabilization effect of SQUID and can be neglected.

B. Coupling of interfacial magnetic phases resulting two-step magnetization and giant exchange bias in the hybrids:

The tuning of diamagnetic or weakly paramagnetic MoS_2 into a giant coercive material has been achieved in this case by ultrathin AFM layers of β-NiOOH phase. For this purpose, we measured ZFC MH hysteresis loops of the two samples in ±5T magnetic field with a field ramp rate of 100 Oe/s. The low temperature (1.8-20K) data (**Fig. 7a**) resemble a strong antiferromagnetic phase along with charge-transfer-induced FM phase arising from interfacial MoS_2 layer that did not let the magnetic moment saturate even until 5T strong field. The interlayer exchange coupling (IEC) arises due to overgrown, thick AFM β-NiOOH layers interacting with MoS_2 sheet is still present in the low field region of HC sample (Inset of **Fig. 7a**). Moving to high temperature region (100-300K), observation of ZFC exchange bias with temperature driven spin canting of antiferromagnetic at the surface is noticed. In the disordered surface and defect of MoS_2 can lead to such high coercive fields. Quantitatively, average coercive fields are evaluated here, by the formula

$$H_C = \left(\left|H_C^+\right| + \left|H_C^-\right|\right)/2$$

where, where $|H_C^+|$ and $|H_C^-|$ are the magnitude of positive and negative bias coercive fields in Oe respectively. This is defined as the half-width of the MH loop at the average of the zero field intercepts and $\langle H_C \rangle$ represents a non-trivial dependence with temperature (Inset of **Fig. 7b**). The strength of exchange bias is calculated by

$$H_{EB} = \left(H_C^+ + H_C^-\right)/2,$$

where polarity of the field is also considered. It is interesting to note that ZFC exchange bias becomes maximum at around 70K with giant magnitude of -1527 Oe which is astonishingly high in any MoS_2 based 2D hybrid system made so far. Upon increasing the temperature (around 300K), it gradually reaches towards zero due to high thermal agitation near room temperature. This behavioral observation becomes clearer if we plot the isothermal $\partial M/\partial H$ vs. *T* for HC at different temperatures (**Fig. 7c**). The strong asymmetric derivative plot @1.8K shows large exchange correlations, witnessing butterfly like splitting near low bias fields. With rising temperature, component of canted AFM spin (from β-NiOOH phase) rises and ZFC EB becomes strongest at around 70K which is also near to the transition temperature of HC sample (MN-1).

Recently, it has been found that surface pinned uncompensated moments at the FM/AFM interface play a dominant role in generating exchange bias and its magnitude.[71-74] When the AFM layer is thinned down over 2D surface, what change occurs is evident from the MH loop of sample MN-2 (**Fig. 7d**). At the lowest temperature 1.8K, enormous average coercive field $\langle H_C \rangle$ of 6439 Oe has been achieved from an ultrathin AFM layer of β-NiOOH/MoS_2 interface. The saturation nature of magnetization at the highest 5T field represents an overall strong FM ordering in this phase which is confirmed by fitting initial growth of magnetization data with Law of

View Article Online
DOI: 10.1039/D5MA00565E

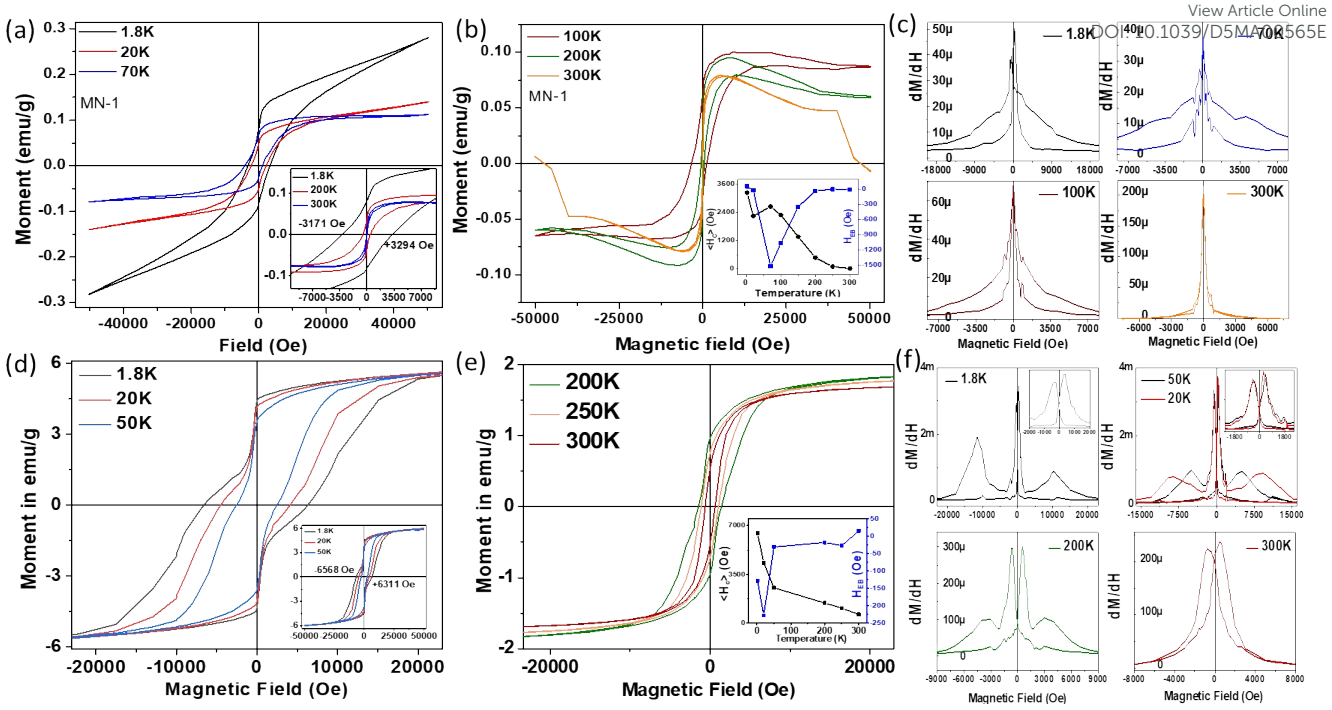

Fig. 7: (a) *MH hysteresis loop for MN-1 in the low temperature range. Inset showing the magnified loops near the zero-field region.* ***(b)*** *MH loop for MN-1 in the high temperature region with strong interlayer exchange effect which gives waist restricted hysteresis loop. The inset shows a variation of average coercivity (H_C) and exchange bias (H_{EB}) with temperature for MN-1.* ***(c)*** *dM/dH plots at different temperature to understand the interlayer exchange effect (splitting near zero field region). The IEC effect is maximum at 70K for MN-1.* ***(d)*** *MH hysteresis loop for MN-2 at low temperature with inset showing complete ferromagnetic saturation at higher fields. Two step magnetizations can be viewed from the nature of the curve.* ***(e)*** *high temperature hysteresis loop. Inset depicts the variation of <Hc> and H_{EB} with temperature in this case.* ***(f)*** *dM/dH plots at different temperatures. Clear asymmetric nature and two peaks are observed due to FM-AFM coupling and two step magnetization process. Unlike MN-1, here the splitting exists until 300K due to evolution of very strong ferromagnetic ordering in the heterostructure.*

approach to saturation magnetization (LAS) in this case [**Fig. S3** in supporting information]. This strong spin exchange coupling between the itinerant AFM layer and charge transfer induced FM order parameter produces this giant coercive field in such composite system. In addition to this, the defective, highly strain induced MoS_2 layers act as robust pinning sites of the surface canted spins. As a result, two step magnetization curves have been found prominently in the lower temperature range of MN-1. [74] As the epitaxial strain in MoS_2 for thin β-NiOOH phase is larger, charge transfer induced FM phase is additionally supplemented by the surface pinned AFM states. We have exploited the interfacial magnetism by virtue of epitaxial strain, charge transfer hybridization and defects etc.[75-78] while in case of thinner phase, this two-step magnetization sustains until 200K (**Fig. 6e**), above which thermal energy weakens the interaction. The natures of variation of E_B and H_c with temperature are given in the inset of **Fig. 7 b,e**.

The presence of coexisting soft and hard magnetic phases (independent) can, in some systems, lead to such two-step magnetization behaviour. However, to further verify whether interfacial exchange coupling plays a dominant role in our system, we have also performed field-cooled (FC) MH measurements for the MN-2 sample at 1.8K shown in **SI Fig. S6**. As shown in the, the FC MH loop for MN-2 exhibits a clear horizontal shift with respect to the zero-field axis, which is a characteristic signature of exchange bias. This shift directly confirms the presence of interfacial exchange coupling between the ferromagnetic (FM) MoS_2 phase and the antiferromagnetic (AFM) β-NiOOH layer, rather than independent behaviour of soft and hard magnetic phases. If the double hysteresis loop was originated purely from coexisting soft and hard magnetic regions with no interfacial coupling, the FC M-H loop will not exhibit an exchange bias shift. Field cooling has induced unidirectional anisotropy, pinning the AFM surface spins, resulting in a horizontal shift of the FC MH loop.

The asymmetry in the positive and negative field-bias can be clearly observed in the $\partial M/\partial H$ plot for MN-2 in **Fig. 7f**. Two prominent peaks arise near the low bias field only in the derivative plots which exist up-to 200K. At 300K, there is only one large splitting is observed due to high thermal energy.

The induced ferromagnetism in our system predominantly originates from interfacial exchange coupling between the weakly antiferromagnetic β-NiOOH and MoS_2. In the MN-2 sample, where the β-NiOOH layer is very thin (~3.5-5 nm), the interface is more exposed, enhancing the proximity effect and leading to stronger interfacial magnetization. In contrast, the thicker β-NiOOH layer in MN-1 (~20 nm) results in weaker interface contribution due to partial screening. However, our XRD and strain analysis (Fig. 2, Table I) reveal significant out-of-plane uniaxial tensile strain in MoS_2, especially in MN-2, which alters interlayer spacing and modulates spin interactions beyond just the interface. Thus, while the magnetism is primarily interfacial, strain-induced changes in the MoS_2

View Article Online
DOI: 10.1039/D5MA00565E

structure also contribute, making the overall MoS_2 thickness relevant to the observed magnetic properties.

4. Thermoremnant-magnetization memory effect studies

A. Thermally induced read/write memory states:

The presence of high exchange bias and coercivity in the 2D hybrid composite suggests the possibility of memory effect due to strong interaction among the magnetic nanoclusters.[79, 80] To verify this, we have investigated in detail a set of measurement protocols for defining the memory states. At first, the MN-2 sample is field cooled (200 Oe) from 300K at a constant cooling rate of 2 K/min. In the temperature range from 70 to 10K, at 20K interval, field is kept off for t= 1 h to create temporary memory steps (fall) in the magnetization process. This can be equivalent to 'writing' process in the system. At designated temperatures it is possible to create such steps and each level of state represents each value. During this wait time (t_w), magnetization relaxes downward as the field is switched off. After 1h, the field is switched on again and cooling continues until further steps are reached. By measuring in this way, we obtained cooling curve until 1.8K (blue color curve in **Fig. 8a**). After reaching 1.8K, the cycle is completed by heating continuously at the same rate without halting at any intermediate temperature (Red curve). Surprisingly, the return magnetization (heating process) also follows the same steps created at the particular exact temperatures during cooling. This tracing can be compared to 'reading' effect in memory process. By just scanning a thermal scan with low field, the states can be read. This temperature-based magnetization state is called thermoremnant memory effect which is newly achieved for 2D hybrid systems by interfacing AFM ultrathin layers. It is to be noted that, in contrast to field, which is usually a control parameter for memory, here thermal energy is used to embed and trace the memory effect in this hybrid heterostructures.[81, 82]

B. Fitting of magnetization dynamics in long relaxation process under different perturbations

To understand the origin of memory dynamics of this hybrid system, it is important to measure long relaxation process. For this, the sample is ZFC cooled from 300K, at a cooling rate of 2k/min and reaches 240K, which is set as the base temperature here (T_0). A low magnetic field of 200 Oe is applied, and time evolution of magnetization is recorded initially for 2000 sec. (t_1). After t_1, the temperature is quickly heated to 250 K ($T_0+\Delta T$) and magnetization continues for another 2000 seconds (t_2). After this, the initial temperature T_0 is kept back and t_3 continues. Like this, we ramped up the temporary heating and retraced back for 11 cycles (t_{11}) as shown in **Fig. 8b**. Every time the temperature is increased for 20K increments and returned back to 240K (T_0). Soon after switching on the field, magnetization grows exponentially up-to t_1. During the intermediate time t_2, as temperature is changed (ΔT), level of moment changes with relaxing independently. As soon as initial temperature T_0 is returned, moment-level returned back to the same value before temporary heating. Interestingly, t_3 is a continuation of t_1 and found to be independent of t_2. It is pertinent to mention that, as time passes, the value of ΔT enhanced. From t_6 onward, even after returning to T_0, the level did not match (differentiated by two colour regions), and large thermal ramping deletes the memory states (re-initialized). For conventional thermoremnant materials, even small positive temperature cycling destroys the memory effect, but due to robust exchange coupling in this MoS_2-hybrid system, it withstands the positive temperature cycling from 240-270K temperature region. For better explicit way, we fitted the magnetization dynamics as a function of time by stretched exponential behavior as follows [67, 68]:

$$M(t) = M_0 - M_r \exp\left[-\left(\frac{t}{\tau}\right)^{\beta}\right] \quad \text{.....(1)}$$

Here M_0 is the temperature independent ferromagnetic component, M_r is the remanent magnetization and τ is the relaxation time. The 'interaction parameter' β lies between 0 and 1. We used this eq. to fit the relaxation process for time period of t_1, t_3 and t_5 in the same time scale. Even after forced temporary heating, the magnetization from different time zones follows the same curve as the initial condition (T_0) is returned back (**Fig. 8c**) i.e. t_5 is a continuation of t_3 and t_1. Inset of **Fig. 8c** shows fitting of t_1 with Eq. 1. The parameters obtained from this fitting also match well for the 3 time zones despite their intermediate different parameter conditions.

C. Simultaneous effect of temperature and field-ON/OFF on memory states

To further test the strength of the memory state, we also performed opposite forced relaxations by switching ON or OFF the magnetic field during temporary cooling period (T_0-ΔT). This is to perform large jump the magnetization level from the initial value (T_0) by ΔT through switching off the field strength (B=0) and let the system relax in the opposite direction (**Fig. 8d**). This is done at 300K to test the room temperature applicability of the samples for practical applications. At the initial condition, i.e. t=0, the field is set on so that the initial moment rises to magnetize the spins in the external field direction for a time period t_1 (2200 s). After then a large jump is occurred due to B=0 and relaxes for another t_2 (2200 s) in the opposite direction. Despite such a large jump in magnetization (large dips in the magnetization plot), when the initial conditions (i.e. T_0, B values) are re-applied, the magnetization level quickly reaches its previous value and continues to grow exponentially following the same path of t_1. We continued the temporary cooling ((T_0-ΔT)) for consecutive 7 cycles (257 h i.e. for long 11 days) and memory level was matched exactly every time proving the stability and robustness of the sample-memory over time and cycles. Hence, the effect of temporary cooling on the sample is to strengthen the memory irrespective of external field dependency. This experiment also shows the robustness of the hybrid against external field conditions in-terms of cyclibility and stability.

D. Re-initialization of the memory states (erasing effect):

So far, the history of magnetization has been preserved by temporary cooling as discussed in the previous experiments. Now, to erase the memory state we have performed positive thermal cycling ($T_0+\Delta T$)

View Article Online
DOI: 10.1039/D5MA00565E

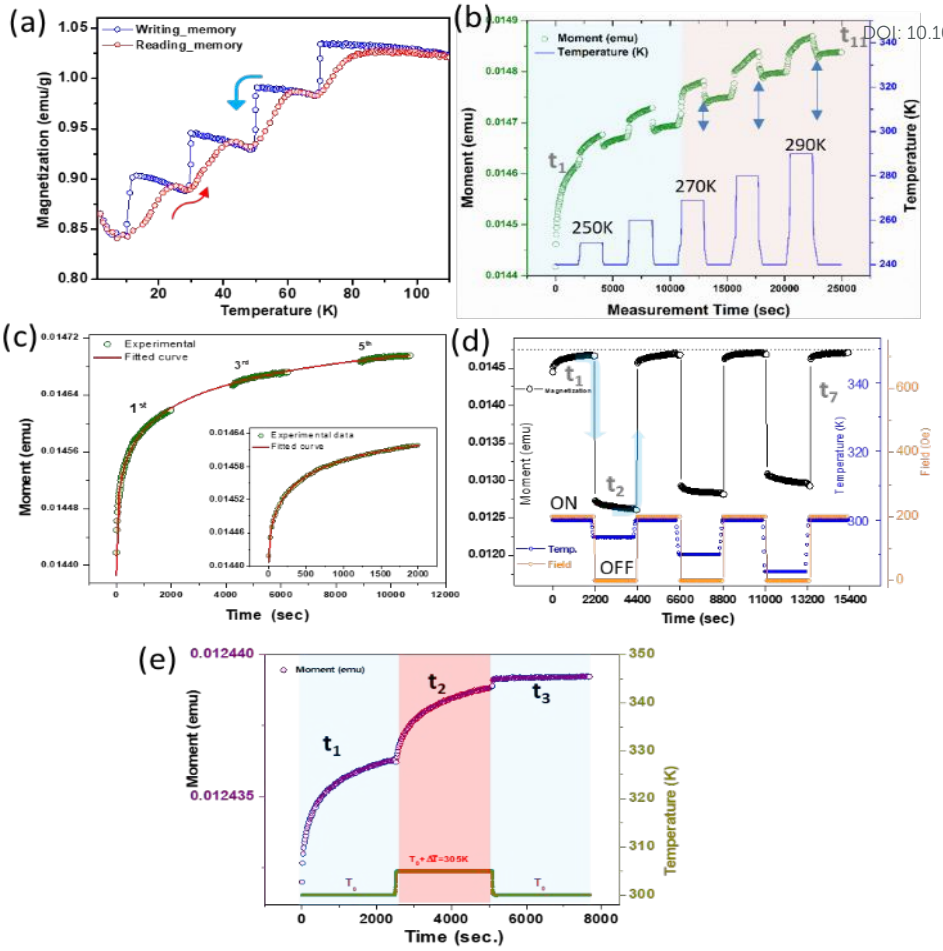

Fig. 8: ***(a)*** *magnetization memory writing-reading process during cooling heating cycles in steps,* ***(b)*** *long relaxation with temporary heating process with increasing temperature. Despite of positive thermal cycle, the memory effect is sustained until 270K.* ***(c)*** *fitting of independent odd thermal cycles with unique stretched exponential curves. Even after intermediate halts, the graphs can be fitted uniformly. Inset shows a complete fit for one cycle with this equation.* ***(d)*** *simultaneous effect of field on/off and variable temperature ramping on the cycles. The level quickly reaches back after the initial condition is retraced back. A total of 7 cycles are performed in this case.* ***(e)*** *re-initialization of memory states by temporary heating process in 3-time domains. By this way heating process, memory can be erased.*

where T_0 is set as 300K and ΔT is just 5K increment in a quick manner to reset the initial conditions which can be similar to erasing memory from the system. As shown in **Fig. 8e**, during t_1 (2500 s), growth of magnetization is recorded at first (purple curve). Then quickly, the temperature is changed to 305K and magnetized independently for t_2 (2500 S, red region), and finally quenched back to T_0=300K with continuation until t_3. Unlike temporary cooling in the previous section, here the level of magnetization and the nature of variation did not match even when the initial conditions are returned. Hence t_3 is not a continuation of t_1 in this case and completely independent which is related to re-initialize of memory states. The result of small positive thermal cycling is to re-initialize (delete) the memory states which can be compared to erasing process in memory devices. With small thermal agitation at this elevated room temperature, the pre-history is deleted, and the process of magnetization follows a different path.

5. Transport studies of the MoS_2/β-NiOOH junction as non-volatile charge memory device

A. Re-writable I-V characteristics of the hybrid:

To test the capability of the composite as an electrical non-volatile memory device we have used this material as active channel layer in a vertical junction type architecture.[83-85] As shown schematically, (**Fig. 9a**), ITO coated substrate was used as bottom electrode over which a thin uniform layer of the MoS_2 based hybrid was coated (See inset of Fig. 6a for design). We used Ag paste as top electrode with a working area of 2mm^2. The switching behavior of the electrical properties of the formed structure is shown in the current density vs. voltage curve (J-V) in **Fig. 9a**. Near zero bias, initially the device shows low conductivity due to its OFF state (sweep 1). Current density increases with applied bias but remains in OFF state until a threshold voltage (V_{th}) reaches +1.36V, at which the current density increases abruptly and jumps to ON state (sweep 2). This step can be represented as an electrical "writing process" in the device. The ON state continues during sweeps 3, 4 and changes bias to negative side until -1.37V where the high conductivity state is switched back to low conductivity OFF state (sweep 5) and can be related to so-called "erasing process". With further increasing the negative bias until -

View Article Online
DOI: 10.1039/D5MA00565E

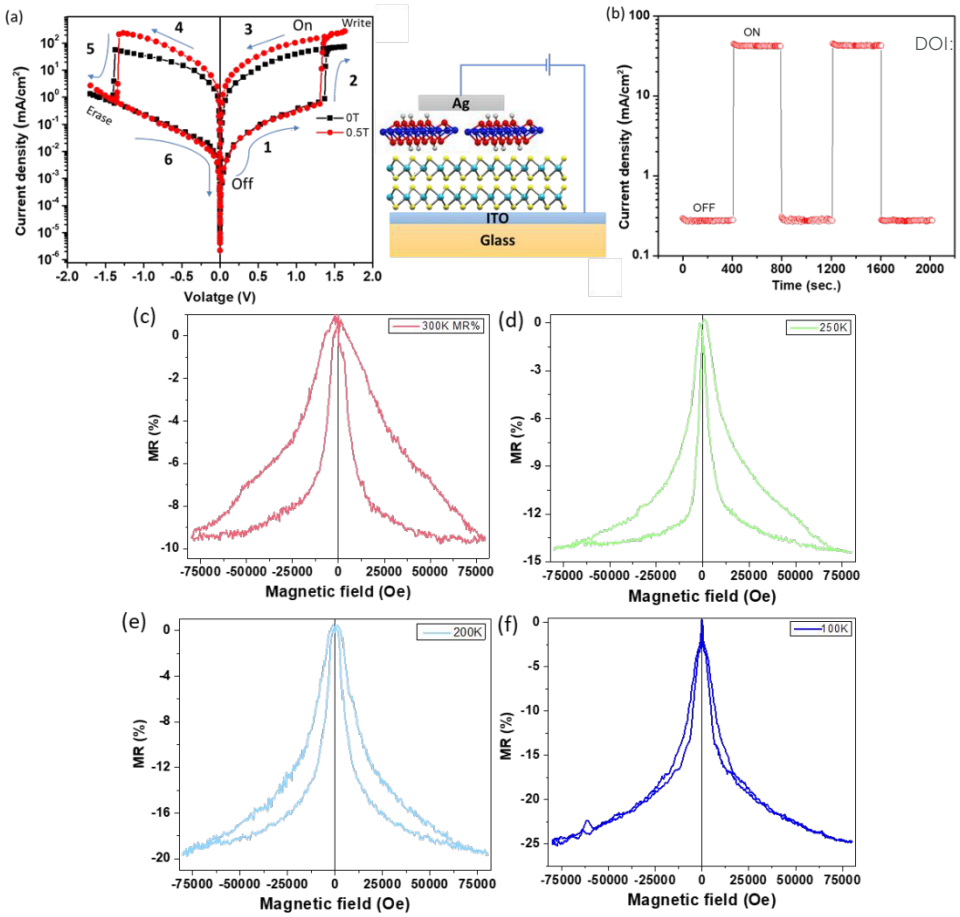

Fig. 9: (a) *Current density vs. voltage curve at different magnetic fields of the sandwich structure made of the composite samples.* ***(b)*** *switching behaviour of ON/OFF state for a complete cycle.* ***(c-f)****: magnetoresistance curve of the composite measured at different temperatures starting from 300K to 100K. Hysteresis is formed during the sweep of magnetic fields.*

1.7V, the OFF state remains stable (readable) and sweeping 6 is completed to back in 0V. During cyclic bias maintain this "write/read/erase" steps are reproduced with stability. It is to be mentioned that we performed the experiment both under zero applied magnetic field (black curve) and 0.5T field (red curve). The ON/OFF threshold voltage and consequently the ON/OFF current ratio are both found to be dependent on the external magnetic field. For zero magnetic field an ON/OFF ratio ~94 was achieved which increased to ~600 at 0.5T which is quite large for 2D MoS_2 based devices. The initial V_{th} was reduced from 1.36V to 1.28V with an application of 0.5T field. The strong dependence of these parameters led us to investigate the conductivity variation with magnetic field i.e., magnetotransport behavior which is given later. To check the stability of the current densities in the OFF and ON states, we ramped the voltages during these states in a cyclic manner as shown in **Fig. 9b.** The first OFF state current density was measured at +0.7V and then ON state value was recorded for another time period. In this way we changed the states and cyclic stability was measured. From the figure it was found that stability was quite good in context to precise switching.

These enhancements likely stem from magnetic field-assisted modulation of the interfacial spin-charge interactions, which in turn affect carrier mobility and trap-mediated conduction pathways within the hybrid layer. Therefore, magnetic field tuning provides an additional control knob to engineer lower operating voltages and sharper memory state separation, marking a promising route toward multifunctional spintronic memory elements.

B. Room temperature large hysteretic magnetoresistance of the hybrid heterostructures:

To understand the role of magnetic state of the two different phases in the conductivity of the overall composite, we measured magnetoresistance of the device in the 2-probe method with application of magnetic field at different temperatures. The percentage change of magnetoresistance (%MR) was calculated using the formula of

$$\%MR = \frac{\rho(\mathrm{H})-\rho(0)}{\rho(0)} \times 100$$

where *ρ(H)* and *ρ(0)* are the resistivity of the composites in presence and absence of magnetic field H. Starting from 300K (**Fig. 9c**), negative magnetoresistance is observed with a hysteresis when the following magnetic field cycling is performed. First the field is increased from 0 Oe to maximum +75 kOe. When returned to 0 Oe, the resistivity followed a different path (lowered value). When the polarity of the field is changed i.e. 0 to -75 kOe, the change is almost

symmetric with hysteresis loop. The MR% with lowering temperature increases from 9.4% (300K) to 25.1% (100K) (**Fig. 9 c-f**) but the hysteresis disappears almost at 100K (only existed near zero field regions). MoS_2 being a diamagnetic/nonmagnetic material, observation of 25% MR value with huge hysteresis is immensely applicable for spintronics applications. Previously, there was report of negative MR effect (-12.7% @ 90 kOe) in thin layer MoS2 gated with CoFe2O4 (CFO) which has a strong ferromagnetic/ferrimagnetic phase.[86] But, in this report vanishing of MR occurs when the layer number is increased. In our case, the pristine β-NiOOH is weakly antiferromagnetic in nature and when surfaced to MoS_2, gives a large hysteretic MR even at 300K. Considering the fact that MoS_2 has overall good semiconducting conductivity, and the β-NiOOH phase is insulator (dielectric), which will not divert the electrical current away from MoS_2. The MR effect in this case may have originated from the proximity induced magnetism in MoS_2 layer by the nearby magnetic insulator of β-NiOOH phase. This effect is highly dependent on the interfacial magnetization of the heterostructure.

The important part is the MR% becomes larger at lower temperature but hysteresis loop is maximum at 300K. The essential hysteresis in MR is the manifestation of dependence of magnetic state with the itinerant conduction electron. Earlier some weak hysteresis was reported in rare earth manganites.[87,88] However, in those cases the low temperature occurrence of hysteresis was explained by spin dependent tunneling across dielectric spacer or formation of ferro-antiferro-ferro tunnel contacts. From our case, the magnetic study already revealed induced magnetization in MoS_2 by the weak AF β-NiOOH phase. Hence in our case the inter-granular tunneling can be approximated by layer surface model, where ferromagnetic (induced) and antiferromagnetic phase are separated by anti-phase boundary (APB).[89,90] At a fixed temperature, when the magnetic field is applied (0 to H_{max}), the surface spins (in β-NiOOH) are pinned according to the nearer spins of FM grains (MoS_2), hence reducing the resistance of the system as ordered system faces less scattering. While the field is lifted off (H_{max} to 0 Oe) the surface spins remain pinned to the nearest moment of inner layer, so the return path follows a hysteresis. With decrease in temperature, the effect of surface spin fluctuation is diminished, and a short-range ordering is formed among the surface spins (cluster formation).[91,92] At lower temperature, the cluster or disordered spins diminish the possibility of spin pinning at the surface and eventually hysteresis area decreases. It is to be noted that due to the semiconducting nature of the MoS_2–NiOOH composite, the resistance of the sample increases significantly at temperatures lower than 100 K. As a result, the resistance level at these temperatures exceeded the measurable limits of our standard PPMS system in the two-probe configuration, preventing reliable MR measurements below 100 K. Despite this, we have provided robust MR data down to 100 K and detailed magnetization data to highlight the evolution of magnetic behaviour at low temperatures, which still allow for a meaningful qualitative correlation between structural, magnetic ordering, and magnetotransport effects.

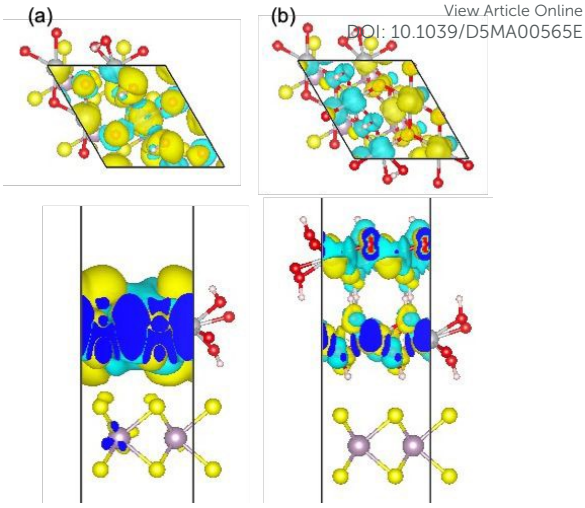

***Fig. 10**: Top and side views of the spin density distributions of (a) monolayer β-NiOOH on MoS_2 and (b) bilayer β-NiOOH on MoS_2. The purple, yellow, grey, red and white balls represent Mo, S, Ni, O, and H, respectively. The black line represents the unit cell boundary.*

6. Density functional theory (DFT) calculations of the MoS_2/β-NiOOH composite

Computational Details:

The first principles calculations were performed with the VASP code[93]. We used the projected augmented wave (PAW) method[94]. For the exchange and core-functional, we used Perdew-Burke-Ernzerhof (PBE) functional[95,96]. The plane wave energy cutoff was set to 400 eV. The dispersion correction was included via the Grimme's D3 (BJ) method[97]. The length of the surface lattice vector of the hexagonal MoS_2 and β-NiOOH cell is 6.38 Å and 5.62 Å, respectively, which has a 12 % mismatch. To construct the composite, we expanded the β-NiOOH cell to match the MoS_2 cell. The thickness of the vacuum layer is more than 20 Å. The k-point was sampled by a gamma-centered 2×2×1 grid. All the atoms were optimized until the force becomes smaller than 0.01 eV/Å.We performed DFT calculations to elucidate the spin state of the MoS_2/β-NiOOH composites. β-NiOOH monolayer and bilayer were optimized on the MoS_2 sheet as shown in Fig. 10. The computational details can be found in the Supporting Information.

It is known that the antiferromagnetic state is stable for the bulk β-NiOOH[98]. The bilayer β-NiOOH on MoS_2 also showed an antiferromagnetic ground state in this case. However, the monolayer MoS_2 showed the ferromagnetic ground state, where the β-NiOOH sheet is spin-polarized. This spin polarization induces a small spin density on MoS_2, indicating the emergence of the 2D ferromagnetism. Furthermore, the bader charge analysis tells us that 0.03e was transferred from MoS_2 to β-NiOOH, which is consistent with the X-ray structural analysis.

View Article Online
DOI: 10.1039/D5MA00565E

6. Conclusion:

In contrast to the classical exchange bias, as typically found in FM/AFM interface, where uncompensated moments are localized and pinned by the AFM surface phase, here we intertwined weak AFM phase with layer dependent 2D MoS_2 surfaces by creating a flat interface. By tuning the thickness of the AFM β-NiOOH phase on top of 2D MoS_2, a competition between interfacial effect (surface) and bulk structure (depth) is created which enables a long-range magnetic exchange interaction in the hybrid heterostructures with large ZFC exchange bias (1500 Oe) and large coercive field (6439 Oe) in the 2D MoS_2 based heterostructures in a new way. The spin interaction model is described by the presence of excellent thermally stable, thermoremanent memory effect in this hybrid structure which shows robust memory states those are easily controllable by temperature rather than conventional magnetic field intensity or polarity. The localized spin moments from the weak AFM counterpart, scatter with the conduction electron of the 2D spacing layer (here MoS_2) and give rise to a hysteretic MR effect of about 25% during charge transport which could be useful in 2D based spintronics applications. Further, non-volatile electrical memory effect has also strongly persisted upon creating a vertical type of junction-structure with simple metallic electrodes as injection of charge carriers in to the layers and interface. The low ON-OFF threshold voltage (~1.25 V) and very high ON/OFF ratio (~6×10^2) are promising in energy efficient 2D MoS_2 based hybrid materials as switching/memory applications. The results are corroborated with disorder field in 2D MoS_2 that can be controlled by the adjacent antiferromagnetic lattice and directly influences the exchange correlation due to proximity effects.

Conflicts of interest

There are no conflicts of interest to declare from the authors

Data availability

Raw Data related to the manuscript are available from the authors upon reasonable request.

Acknowledgements

S.B acknowledges Japan Society for the Promotion of Science (JSPS) for providing JSPS International postdoctoral fellowship (standard) (ID P20070) during initial stages of this work. Researcher S.B conducts his research under the Marie Skłodowska-Curie Actions – COFUND project, which is co-funded by the European Union (Physics for Future – Grant Agreement No. 101081515) at FZU. H.T. and S.B thanks JSPS for supporting via Grants-in-Aid for Scientific Research (KAKENHI Project Numbers 22H00315 and 22F20070). I.A.K acknowledges the support from the Operational Programme Johannes Amos Comenius financed by European Structural and Investment Funds and the Czech Ministry of Education, Youth and Sports (Project No. SENDISO CZ.02.01.01/00/22_008/0004596).

Disclaimer

Project Co-funded by the European Union. Views and opinions expressed are however those of the author(s) only and do not necessarily reflect those of the European Union or European Research Executive Agency. Neither the European Union nor the granting authority can be held responsible for them.

References

1 K. S. Novoselov, A. Mishchenko, A. Carvalho, A. H. Castro Neto, *Science*, 2016, **353**, 9439.

2 D. Voiry, et al. *Nano Lett.*, 2013, **13**, 6222–6227.

3 J. Kibsgaard, Z. Chen, B. N. Reinecke, and T. F. Jaramillo, *Nat. Mater.*, 2012, **11**, 963–969.

4 B. Radisavljevic, A. Radenovic, J. Brivio, V. Giacometti, and A. Kis, *Nat. Nanotech*., 2011, **6**, 147–150.

5 B. Radisavljevic, M. B. Whitwick, and A. Kis, *ACS Nano*, 2011, **5**, 9934–9938.

6 H. Nam, *ACS Nano*, 2013, **7**, 5870–5881.

7 D. J. Late, et al. *ACS Nano*, 2013, **7**, 4879–4891.

8 A. Castellanos-Gomez, et al. *Nano Lett.*, 2013, **13**, 5361–5366.

9 B. Scharf, G. Xu, A. Matos-Abiague, I. Zutic, *Phys. Rev. Lett.*, 2017, **119**, 127403;

10 X. Liang, L. Deng, F. Huang, T. Tang, C. Wang, Y. Zhu, J. Qin, Y. Zhang, B. Peng, L. Bi, *Nanoscale*, 2017, **9**, 9502.

11 W. Zhang, L. Zhang, P. K. J. Wong, J. Yuan, G. Vinai, P. Torelli, G. van der Laan, Y. P. Feng, A. T. S. Wee, *ACS Nano*, 2019, **13**, 8997.

12 X. Liu, C Z Wang, Y X Yao, W C Lu, M Hupalo, M C Tringides and K. M. Ho, *Phys. Rev. B*, 2011, **83**, 235411.

13 Y. S. Dedkov and M. Fonin, *New J. Phys*., 2010, **12**, 125004.

14 T. P. Kaloni, N. Singh and U. Schwingenschlogl, *Phys. Rev. B*, 2014, **89**, 035409.

15 A. V. Krasheninnikov, P. O. Lehtinen, A. S. Foster, P. Pyykko and R. M. Nieminen, *Phys. Rev. Lett.*, 2009, **102**, 126807.

16 T. P. Kaloni, J. Phys. Chem. C, 2014, 118, 25200

17 S. P. Tsai, C. Y. Yang et. Al. *Adv. Quantum Technol.*, 2021, **4**, 2000104.

18 A. J. Tkalych, K. Yu, and E. A. Carter, *J. Phys. Chem. C,* 2015, **119**, 43, 24315–24322.

DOI: 10.1039/D5MA00565E

19 A. J. Tkalych, H. L. Zhuang, E. A. Carter, *ACS Catal.,* 2017, **7**, 8, 5329–5339.

20 Y. Hao, J. Li, X. Cao, L. Meng, J. Wu, X. Yang, Y. Li, Z. Liu, M. Gong, *ACS Catal.,* 2023, **13**, 5, 2916–2927.

21 E. W. Jungner, Anordning Vid Elektroder for Elektriska Accumulatorer. *Swedish Patent* 1897, 8558.

22 E. W. Jungner, Electrode for Reversible Galvanic Batteries. *U.S. Patent* 1908, 884, 930.

23 H. Bode, K. Dehmelt, J. Witte, *Electrochim. Acta* 1966, **11**, 1079−1087.

24 R. Oesten, M. Wohlfahrt-Mehrens, S. Ströbele, M. Kasper, R. A. Huggins, *Ionics*, 1996, **2**, 293−301.

25 A. Szytula, A. Murasik, M. Balanda, Phys. Status Solidi B, 1971, **43**, 125−128.

26 R. Barnard, C. F. Randell, F. L. J. Tye, *Appl. Electrochem.,* 1980, **10**, 109−125.

27 Q. Song, Z. Tang, H. Guo, S. L. I. Chan, *J. Power Sources*, 2002, **112**, 428−434.

28 Y. F. Li, A. Selloni, *J. Phys. Chem. Lett.* 2014, **5**, 3981−3985.

29 A. J. Tkalych, K. Yu and E. A. Carter, *J. Phys. Chem. C*, 2015, **119**, 24315–22.

30 H. Jeong, J. Y. Kim, J. W. Kim, J. Hwang, J. E. Kim, J. Lee, T. Yoon, B. Cho, S. Kim, R. Ruoff, S. Choi, *Nano Letters*, 2010, **10**, 4381.

31 S. Hong, J. Kim, S. Kim, S. Choi, B. Cho, *IEEE Electron. Device Lett.*, 2010, **31**, 1005.

32 S. Hong, J. Kim, S. Kim, B. Cho, *J. Appl. Phys.,* 2011, **110**, 044506.

33 L. Wang, W. Yang, Q. Sun, P. Zhou, H. Lu, S. Ding, D. Zhang, *Appl. Phys. Lett.* 2012, **100**, 063509.

34 T. Jonsson, J. Mattsson, C. Djurberg, F. A. Khan, P. Nordblad, and P. Svedlindh, Phys. Rev. Lett., 1995, **75**, 4138.

35 P. Jonsson, M. F. Hansen, P. Svedlindh and P. Nordblad, Physica B, 2000, **284**, 1754.

36 Y. Sun and M. B. Salamon, K. Garnier and R. S. Averback, Phys. Rev. Lett., 2003, **91**, 167206.

37 L. Lutterotti, MAUD™ 2002, version 1 85

38 H. M. Rietveld, J. Appl. Cryst., 1969, 2, 65.

39 L. Yang, X. Cui, J. Zhang, *et al. Scientific Reports,* 2014, 4, 5649.

40. A. Le Bail, *Modelling Anisotropic Crystallite Size/Microstrain in Rietveld Analysis*, 1992, **846**, 142-153.

41. R. E. Dinnebier, A. Leineweber and J. S.O. Evans. *Rietveld Refinement: Practical Powder Diffraction Pattern Analysis using TOPAS*, Berlin: De Gruyter, 2019.

42. J. Wei, H. Huang, Q. Luo *et al. Catal Lett.,* **2022**, 152, 263–275.

43. T. Nagarajan, M. Khalid, N. Sridewi, P. Jagadish, Priyanka, S. Shahabuddin, K. Muthoosamy, R. Walvekar, *Scientific Reports,* 2022, **12**, 14108.

44 S. Bhattacharya, D. Dinda, B. K. Shaw, S. Dutta, S. K. Saha, *Physical Review B*, 2016, **93(18)**, 184403.

45 S. Bhattacharya, W. Choi, A. Ghosh, S. Lee, G. D. Lee, S. K. Kim, *Nanotechnology*, 2021, **32**, 385705.

46 S. Bhattacharya, E. Mathan Kumar, R. Thapa, S. K. Saha, *Applied Physics Letters,* 2017, **110**, 032404, 5.

47 C. A. Schneider, W. S. Rasband and K. W. Eliceiri, *Nature Methods*, 2012, ***9*(7)**, 671–675.

48 H. Wang, H. Yuan, S. S. Hong, Y. Lib and Y. Cui, *Chem. Soc. Rev.*, 2015, **44**, 2664.

49 K. D. Rasamani, F. Alimohammadi, Y. Sun, *Materials Today*, 2017, **20**, 2.

50. S. Zhang, Z. Yin, L. Wang et.al. *Energy Mater.,* 2024, **4**, 400065.

51. K. Zhang, P. Li, S. Guo et. Al. *J. Mater. Chem. A*, 2018, **6**, 22513-22518.

52 S. Pak, J. Lee, Y. Lee, A. Jang, S. Ahn, K. Y. Ma, Y. Cho, J. Hong, S. Lee, H. Y. Jeong, H. Im, H. S. Shin, S. M. Morris, S. Cha, J. I. Sohn, and J. M. Kim, *Nano Letters,* 2017**, 17** (9), 5634-5640.

53 J. U. Lee, S. Woo, J. Park, H. C. Park, Y. W. Son and H. Cheong, *Nature Communications*, 2017, **8**, 1370.

54 C. Cai, Z. Tao, Y. Zhu, Y. Tan, A. Wang, H. Zhou and Y. Yang, *Nanoscale Adv.*, 2021, **3**, 3780-3787.

55 P. N. Ghosh and C. R. Maiti, *Physical Review B*, 1983, **28**, 2237.

56 A. Molina-Sánchez and L. Wirtz, *Physical Review B,* 2011, **84**, 155413.

57 T. Li and G. Galli, *J. Phys. Chem. C*, 2007, **111**, 44, 16192–16196.

58 B. Pacakova, J. Vejpravova, A. Repko, A. Mantlikova, M. Kalbac, *Carbon*, 2015, **95**, 573-579.

59 M. Sadeghi, A. Zelati, S. Rezaee, C. Luna, R. Matos, M. Pires, N. Ferreira, H. Fonseca Filho, A. Ahmadpourian, Ş. Ţălu, *Coatings*, 2022, **12(9)**, 1364.

60 M. Rajput, S. K. Mallik, S. Chatterjee, A. Shukla, S. Hwang, S. Sahoo, G. V. Pavan Kumar and A. Rahman, *Communications Materials*, 2024, **5**, 190.

61 M. Baker, R. Gilmore, C. Lenardi and W. Gissler, *Appl. Surf. Sci*., 1999, **150**, 255–262.

62 In S. Kim, V. K. Sangwan, D. Jariwala, J. D. Wood, S. Park, Kan-Sheng Chen, F. Shi, F. Ruiz-Zepeda, A. Ponce, M. Jose-Yacaman, V. P. Dravid, T. J. Marks, M. C. Hersam, and L. J. Lauhon, ACS Nano, 2014, **8 (10)**, 10551-10558.

63 A. Curcio, J. Wang, Z. Wang, Z. Zhang, A. Belotti, S. Pepe, M. B. Effat, Z. Shao, J. Lim, and F. Ciucci, *Adv. Funct. Mater.* 2021, **31**, 2008077.

64 D. Ko, X. Jin, K.-d. Seong, B. Yan, H. Chai, J. M. Kim, M. Hwang, J. Choi, W. Zhang, Y. Piao, *Appl. Catal. B: Environ.* 2019, **248**, 357.

65 Y. Li, Y. Yu, Y. Huang, R. A. Nielsen, W. A. Goddard, Y. Li, L. Cao, *ACS Catalysis* 2015, **5**, 448.

66 M.-R. Gao, J.-X. Liang, Y.-R. Zheng, Y.-F. Xu, J. Jiang, Q. Gao, J. Li, S.-H. Yu, *Nat. Commun*. 2015, **6**, 5982.

67 G. M. Wang, Y. C. Ling, X. H. Lu, T. Zhai, F. Qian, Y. X. Tong and Y. Li, *Nanoscale*, 2013, **5**, 4129–33.

68 S. Narayanaru, H. Kuroki, T. Tamaki, G. M. Anilkumar and Takeo Yamaguchi, *RSC Sustainability*, 2025, **3**, 1705.

69 N. Weidler, J. Schuch, F. Knaus, P. Stenner, S. Hoch, A. Maljusch, R. Schäfer, B. Kaiser, and Wolfram Jaegermann, *J. Phys. Chem. C*, 2017, **121 (12)**, 6455-6463.

70. C. Mahala, M. Devi Sharma, M. Basu, *ChemElectroChem* 2019, **6**, 3488.

71 H. Ohldag, A. Scholl, F. Nolting, E. Arenholz, S. Maat, A. T. Young, M. Carey and J. Stohr, *Phys. Rev. Lett.*, 2003, **91**, 017203.

72 I. K. Schuller, R. Morales, X. Batlle, U. Nowak, G. Güntherodt, *Journal of Magnetism and Magnetic Materials*, 2016, 416, 2–9.

73 M. Kiwi, Exchange bias theory. *Journal of Magnetism and Magnetic Materials,* 2001, **234**, 584–595.

74 X. Wu, D. Lan, I. Hwang, C. Sun, H. Zhou, X. Yu, P. Yang, X. Yu, C. Liu, P. Chen, J. Ding, J. Chen, G. M. Chow, *Journal of Alloys and Compounds*, 2023, **932**, 167582.

75 M. K. Lee, T. K. Nath, C. B. Eom, M. C. Smoak, F. Tsui, *Appl. Phys. Lett.*, 2000, **77**, 3547–3549.

76 T. L. Meyer, A. Herklotz, V. Lauter, J. W. Freeland, J. Nichols, F. J. Guo, S. Lee, T. Z. Ward, N. Balke, S. V. Kalinin, M. R. Fitzsimmons, H. N. Lee, *Phys. Rev. B*, 2016, **94**, 174432.

77 R. Pentcheva, H.S. Nabi, *Phys. Rev. B*, 2008, **77**, 172405.

78 M. Bibes, J.E. Villegas, A. Barthelemy, *Advances in Physics*, 2011, **60**, 5–84.

79 M**.** Suzuki, I**. S. Suzuki** and M**.** Matsuura, *Phys. Rev. B***, 2006,** 73, 184414.

80 Jan-Ulrich Thiele, Stefan Maat, and Eric E. Fullerton, *Appl. Phys. Lett.*, 2003, **82**, 2859.

81 N. Khan, P. Mandal, and D. Prabhakaran, *Phys. Rev. B*, 2014, **90**, 024421.

82 Y. Sun, M. B. Salamon, K. Garnier, and R. S. Averback, *Phys. Rev. Lett.,* 2003, **91**, 167206.

83 S. Wang, K. Manga, M. Zhao, Q. Bao, K. Loh, *Small,* 2011, **7**, 2372.

84 V. Nagareddy, M. D. Barnes, F. Zipoli, K. T. Lai, A. M. Alexeev, M. Felicia Craciun, and C. David Wright, *ACS Nano,* 2017, **11**, 3, 3010–3021.

85 X. Zhuang , Y. Chen , G. Liu , P. Li , C. Zhu , E. Kang , K. Noeh , B. Zhang , J. Zhu , Y. Li , *Adv. Mater.,* 2010, **22**, 1731.

86 W. Jie, Z. Yang, F. Zhang, G. Bai, C. Wah Leung, and J. Hao, *ACS Nano,* 2017, **11**, 7, 6950–6958.

87 K. A. Shaykhutdinov, S. V. Semenov, D. A. Balaev, M. I. Petrov, N. V. Volkov, *Phys. Solid State*, 2009, **51**, 778– 780.

88 K. A. Shaykhutdinov, S. I. Popkov, S. V. Semenov, D. A. Balaev, A. A. Dubrovskiy, K. A. Sablina, N. V. Sapronova, N. V. Volkov, *Journal of Applied Physics*, 2011, **109**, 053711.

89 D. Tripathy, A.O. Adeyeye, S. Shannigrahi, *Physical Review B*, 2007, **76**, 174429.

90 S. Ghosh, P. C. Patel, P. C. Srivastava, *J Mater Sci: Mater Electron*, 2017, **28**, 15284–15292.

91 E. DeBiasi, R.D. Zysler, C. A. Ramos, H. Romero, D. Fiorani, *Physical Review B*, 2005, **71**, 104408.

92 E. De Biasi, C. A. Ramos, R. D. Zysler, H. Romero, *Physical Review B*, 2002, **65**, 144416.

93. G. Kresse and J. Hafner, *Phys. Rev. B*, 1993, **47**, 558.

94. P. E. Blöchl, Projector Augmented-Wave Method. *Phys. Rev. B* 1994, ***50***, 17953-17979.

95. J. P. Perdew, K. Burke, M. Ernzerhof, *Phys. Rev. Lett.,* 1996**,** ***77***, 3865-3868.

View Article Online
DOI: 10.1039/D5MA00565E

96. S. Grimme, J. Antony, S. Ehrlich, H. Krieg, *J. Chem. Phys.* 2010, **132**, 154104.

97. S. Grimme, S. Ehrlich, L. Goerigk, *J. Comput. Chem.* 2011, **32**, 1456-65.

98. A. J. Tkalych, K. Yu, E. A. Carter, *J. Phys. Chem. C,* 2015, **119**, 43, 24315–24322.

View Article Online
DOI: 10.1039/D5MA00565E

Data availability statement

Data for this article, including experimental datasets including raw data, are available at Mendeley Data at https://doi.org/10.17632/55px8bdhd3.1.

Bhattacharya, Shatabda (2025), "Evolution of Giant Exchange Bias with Ferromagnetic Ordering and Robust Memory Effect by Strain Engineering MoS2 in Weak Antiferromagnetic Gating ", Mendeley Data, V1, doi: 10.17632/55px8bdhd3.1

The data contains raw .txt data files for magnetic measurements, zfc fc files, relaxation curves, xrd files for rietveld analysis, raman data file, transport data for RT, J-V curves, MR data in %, AFM height profile files etc.

With thanks and regards

Shatabda Bhattacharya, Ph.D.

Shatabda Bhattacharya, Ph.D.
MSCA P4F Fellow
FZU-Institute of Physics of the Czech Academy of Sciences
Division of Condensed Matter Physics
Department of Functional Materials
Na Slovance 1999/2, 182 00 Prague 8, Czech Republic
Tel: (+420) 6050 47247
E-mails: shatabda@gmail.com shatabda@fzu.cz
Google Scholar
ID: https://scholar.google.com/citations?user=lL6TDX0AAAAJ&hl=en&oi=ao